Available online at www.sciencedirect.com

ScienceDirect

Procedia CIRP 94 (2020) 5–10

www.elsevier.com/locate/procedia

11th CIRP Conference on Photonic Technologies [LANE 2020] on September 7-10, 2020

On the relationship between the bulge effect and the hot cracking formation during deep penetration laser beam welding

Antoni Artinov[a,*], Marcel Bachmann[a], Xiangmeng Meng[a], Victor Karkhin[b], Michael Rethmeier[c,a,b]

[a] *Bundesanstalt für Materialforschung und -prüfung (BAM), Unter den Eichen 87, 12205 Berlin, Germany*
[b] *Peter the Great St. Petersburg Polytechnik University, Department of Welding and Laser Technologies, 195251 St. Petersburg, Russia*
[c] *Technische Universität Berlin, Departments of Machine Tools and Factory Management, 10623 Berlin, Germany*

- Keynote Paper -

* Corresponding author. Tel.: +49 3081043101; *E-mail address:* Antoni.Artinov@bam.de

Abstract

Recent studies have confirmed the widening of the weld pool interface, known as a bulge effect, during deep penetration high power laser beam welding. The link between such geometric particularities of the weld pool shape and the hot cracking phenomena is significant. The present work seeks to extend the level of understanding by investigating their relationship. A coupled multiphysics, multiscale numerical framework is developed, comprising a series of subsequent analyses. The study examines the influences of the bulge on the three most dominant effects causing hot cracking, namely the thermal cycles, the mechanical loading, and the local microstructure. The bulge in the weld pool shape forms approximately in the middle of the plate, thus correlating with the location of hot cracking. It increases the hot cracking susceptibility by enhancing the three dominant effects. The numerical results are backed up by experimental data.

Keywords: Hot cracking; Bulge effect; Numerical modelling; Laser beam welding; Deep penetration

1. Introduction

Nowadays, the laser beam welding process is an established high-performance joining technology. It brings several technical advantages compared to conventional arc welding methods, such as locally highly concentrated and precise heat input, allowing welding with minimal distortion of large-area components [1]. Thus, laser beam welding is a reliable state of the art joining process, especially for the production of long joints on relatively thin sheets, e.g., rail vehicles, containers, and cars.

With the rapidly increasing availability of higher laser power of up to 100 kW [2], applications in the sheet thickness range of more than 20 mm are reachable [3, 4]. However, as earlier and latest research results show, with increasing welding speed and sheet thickness, defects occur that are untypical for unalloyed and low-alloy steels under conventional welding conditions. These include, above all, hot cracking in the inner part of the weld metal, especially in the area where the crystallization fronts collide [5-8]. The nature of such solidification cracks is highly complex, and only a few material phenomena from the welding field were so thoroughly investigated in the last five decades [9, 10]. The cracks initiate in the fusion zone, at temperatures above the solidus temperature. Solidification shrinkage and thermal contraction lead to a localized stress/strain across the grain boundary liquid

10.1016/j.procir.2020.09.002

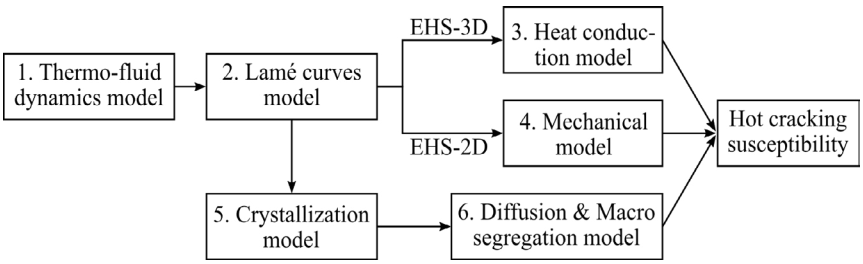

Fig. 1. Scheme of the numerical framework using the concept of an equivalent heat source (EHS) to couple the models

film, which in turn causes their formation [11, 12]. The presence of elements constituting low melting eutectics, such as sulfur and phosphorus and their segregation, can further increase the hot cracking susceptibility by extending the solidification temperature range [13, 14].

A detailed literature review shows that the complex interactions between the thermal, mechanical, and metallurgical factors determine the cracking behavior of the welded part [15].

All these factors are strongly coupled and depend on the weld pool shape and vice versa. The underlying physical phenomena in the weld pool are long known to be crucial for the formation of defects during the solidification stage of the process, e.g., hot cracking [16]. Studies on deep penetration electron beam welding from the early 1980s demonstrate the importance of the weld pool shape on the formation of solidification cracking. The authors examined a widening of the weld pool interface, nowadays referred to as a bulge region, with a delay in the solidification behavior, which in turn led to the formation of cracks within this region [17]. The results show a link between the bulge and the defect occurrence [18, 19]. The influence of the bulge on the thermal cycles and thus on the stress/strain distribution in the cracking region was investigated in [20, 21]. The strong correlation between the bulge region in the weld pool and the formation of hot cracking was confirmed in [22, 23].

The observation and investigation of the bulge effect during the welding process is a highly challenging task due to the optical inaccessibility. Despite this fact, a bulge region can be found in several numerical works, even though not being the object of analysis [24-30]. The latest research experimentally proves the existence of a bulge during laser beam welding of thick sheets by using a specially designed set-up with a transparent quartz glass [31, 32]. To the best of the authors' knowledge, there are only a few research results published on the occurrence of bulging during welding with high power lasers. The correlation between the cracks and the bulge seems to be significant and yet poorly understood. Most attempts to connect the bulging phenomena to hot cracking concentrate on one or two of the dominant factors for crack formation, e.g., the solidification range, the critical stress/strain, and do not examine their complex interactions. Considering the current state of knowledge, the need arises to expand the understanding of these phenomena and their interactions.

The present work seeks to deepen the level of understanding by investigating their relationship. A coupled multiphysics, multiscale numerical framework is developed, comprising a series of subsequent analyses. The study examines the influences of the bulge on the three most dominant effects causing hot cracking, namely the thermal cycles, the mechanical loading, and the local microstructure.

2. Numerical framework

Altogether, six numerical models are linked by one-dimensional coupling in the proposed numerical framework, see Fig. 1.

In step (1), the bulge effect is reproduced in a steady-state thermo-fluid dynamics problem considering the coupling between the melt flow and the heat transfer on a local level. The steady-state weld pool shape is a result of step (1), which according to [33, 34] can be used as an equivalent heat source (EHS) to obtain the global temperature cycles. Step (2) presents a novel approach allowing a 3D reconstruction of the weld pool interface to an EHS. The 3D and 2D temperature fields calculated with the EHS are subsequently used in steps (3) and (4), respectively. The former is used to analyze the steady-state solidification behavior of the melt and the latter as a thermal load for the 2D mechanical model described in step (4). In (5), a technique for calculating the main crystallization parameters, e.g., the geometry of the crystal axis, the growth rate of the crystal, and its cross-sectional area, based on the outcomes from (1) and (2) is derived. The results from (5) are finally utilized in a combined diffusion and macro segregation model in step (6). The model estimates the extended solidification temperature range due to a solute enrichment in the liquid, ahead of the solid-liquid interface. Further details on the single steps of the numerical framework are described in the following subsections.

2.1. Thermo-fluid dynamics model

The thermo-fluid dynamics problem aims to obtain a steady-state solution for a weld pool interface including a bulge region, as experimentally observed in [32]. It includes the coupled solution of the mass and energy conservation equations, the Navier-Stokes equations, and the transport equations for the turbulent kinetic energy and the turbulent dissipation rate. The model is based on several previous works with some further improvements and modifications [35-37].

Here some of the main assumptions will be discussed, whereby further details can be obtained from [38]. In the proposed set-up, the workpiece moves relative to the origin of the Cartesian coordinate system which coincides with the origin of the laser source. A fixed keyhole geometry is utilized in the

model based on the assumption that the recoil pressure in the keyhole is perfectly balanced by the surface tension force. The surface temperature of the keyhole is replaced by the evaporation temperature of the material. This assumes that the temperature inside the keyhole should be at least equal or higher than the evaporation temperature of the material. The approach does not allow to directly consider the effects of the focal position and multiple reflections on the energy absorption. Thus, it is advisable to increase the horizontal cross-sectional area of the conical keyhole in the middle of the plate. This enhances the formation of a bulge in the weld pool shape, especially in the narrow regions around the keyhole. The model considers the most relevant physical effects, such as Marangoni and natural convection, latent heat of fusion, and temperature-dependent material properties up to evaporation temperature.

2.2. Reconstruction of the weld pool interface by Lamé curves

The reconstruction of the numerically obtained weld pool geometry is realized with Lamé curves (superellipses). For this the solid-liquid interface from *2.1* is discretized by a set of data points. The procedure starts by dividing the data into a certain number of levels along the thickness direction of the weld pool. The vertical distance between the planes is variable along the thickness direction improving the approximation of the interface even in the more complex-shaped areas influenced by the thermo-capillary driven flow. The data points in each level are approximated by two Lamé curves, one for the front and one for the rear part of the weld pool.

Every 2D contour in each plane is sufficiently defined by eight parameters. To obtain these at least eight data points are required. However, the accuracy of the approximation is improved by taking more data points. The fitting procedure of the curves makes use of the least square method to optimally reproduce the 2D contour for each level. The algorithm provides the parameters for a single plane and is repeated for each plane. The data in the gaps between two planes are obtained by interpolation between the known values or polynomial fitting. Further details can be found in [39].

2.3. Heat conduction model with an equivalent heat source

The calculated shape parameters of the weld pool interface define the equivalent heat source. This is subsequently applied in a global heat conduction simulation to compute the temperature fields. The algorithm detects the nodes within the EHS and replaces their temperature values by the solidus temperature, thus, assuring an equivalent energy input. The EHS moves with the processing speed in the welding direction. In the 2D case the EHS is moved perpendicular through the two-dimensional plane of interest. This technique allows the coupling of the local thermo-fluid dynamics simulation and the global temperature field. Hence, the influence of the bulge in the weld pool on the thermal history of the part can be investigated.

In addition, it offers high accuracy and efficiency by solving the heat transfer problem during welding compared to common volumetric heat sources, such as the cylindrical heat source model or the conical Gaussian heat source model [21]. More information on the concept of an equivalent heat source can be found in [38-40].

2.4. Mechanical model

A 2D plane strain model is used to examine the mechanical loading on the part. The 2D temperature field from *2.3* is applied as a thermal loading. Hence, the effect of the weld pool shape, and particularly of the bulge region, on the temporal and spatial distribution of the stress/strain can be studied in-depth. The model considers solid-solid phase transformations from ferrite (base material) to austenite during heating and austenite to martensite during cooling. The boundary conditions were obtained experimentally by using the concept of restraint intensity [41]. Therefore, the model considers the influence of the stiffness of the solid material around the weld pool on the stress/strain development during solidification. A full description of the model can be found in [21].

2.5. Crystallization model

The crystallization model in the presented numerical framework is based on previous research from [42]. It considers the movement of the solidification front (tail part of the weld pool), reconstructed numerically by Lamé curves, see *2.2*, using the set of data points computed in *2.1*. The movement and the shape of the solidification front determine the rate and direction of crystallization, which are crucial factors for the final microstructure of the weld and the solute enrichment ahead of the solid-liquid interface. The model is extended numerically to three dimensions based on the following assumptions:

- The crystallization process reaches a steady state, where the solidification front does not change with time.
- The solidification front is defined by the liquidus isotherm.
- The local decrease of the liquidus temperature due to the rising impurity concentration is neglected.
- The direction of crystallization coincides with the direction of the temperature gradient.

2.6. Diffusion & Macro segregation model

Generally, the concentration of impurities, such as sulfur, rises ahead of the solidification front. Thus, the liquidus temperature of the material decreases locally having a great influence on the hot cracking resistance. To determine the local microstructure the mass transfer problem for the sulfur element needs to be solved. The challenge of obtaining a solution to this problem is the concentration discontinuity at the solid-liquid interface, defined by the distribution coefficient. This challenge is overcome by making use of the concept of mass transfer potential and solubility of the impurity element [43]. The mathematical formulation presented in [43] is further extended to consider temperature-dependent solubility and diffusion coefficients of the sulfur element in both solid and liquid state. The basic assumptions remain hereby unchanged. The model uses the outcomes from *2.1-2.3* and *2.5*, the reconstructed shape of the solidification front, the crystal axis and cross-

sectional profile, the solidification rate, the space and time-dependent temperature distribution along the crystal axis, etc. as input data.

3. Experimental procedures

The numerically obtained results were validated by experimental data from several experiments. These included temperature measurements with thermocouples, thermal imaging cameras, and a high-speed camera. The geometrical dimensions of the computed weld pool were compared to metallographic cross-sections along the weld and numerically estimated weld end crater shape [44]. The restraint intensity was obtained by a Controlled Tensile Weldability test (CTW). Additional horizontal sections on the top surface were used to validate the crystallization model. Further details about the single experiments is given in the references cited in *2.1-2.6*.

4. Results & Discussion

Three factors, namely the thermal cycles, the mechanical loading, and the local microstructure are identified as decisive for the determination of the cracking behavior of the welded part. The results in the following subsections are structured in such a way that the influence of the bulge effect on every single factor is estimated and analyzed. Furthermore, their correlation to the decrease in hot cracking resistivity is studied.

4.1. Influence of the bulge on the thermal factor

The bulge effect was numerically obtained in the thermo-fluid dynamics model presented in *2.1*. It is part of the three-dimensional weld pool interface computed by the model, see Fig. 2a. The results show a bulge effect in both the cross and longitudinal sections, see Fig. 2b and 2c. The shape and size of the bulge are mainly defined by the thermo-capillary effect in the upper and lower part of the weld pool, highlighted in Fig. 2b. These flows ensure mass conservation by bringing part of the cooled material back to the vicinity of the keyhole, causing two necking areas. The combination of these flows, also known as Marangoni flows, and the relative movement of the laser source to the workpiece results in the formation of this geometrical particularity.

For the analysis of the bulge on the thermal factor the results from both the local temperature field calculated in *2.1* and the global temperature field calculated in *2.3* can be used. Here the results from *2.1* are preferred since they provide additional data

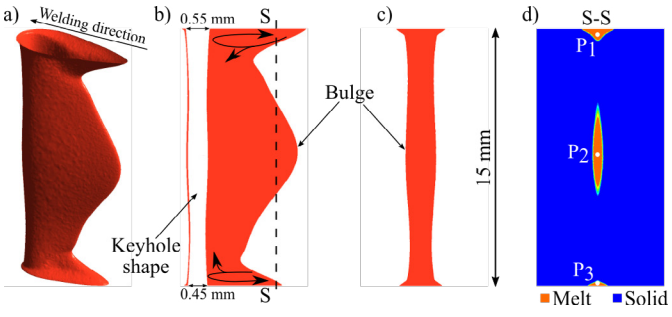

Fig. 2. Results from the thermo-fluid dynamics model: a) three-dimensional weld pool interface, b) longitudinal section of the weld pool in the symmetry plane, c) cross-section of the weld pool and d) liquid metal in the cross-section S-S according to [21, 32]

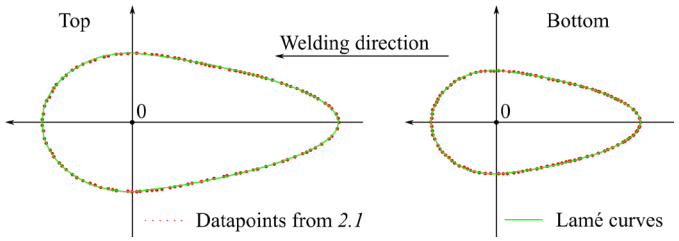

Fig. 3. Reconstructed weld pool shape on the top and bottom surfaces by Lamé curves according to [39]

from inside the weld pool. Therefore, an exemplary reconstruction of the top and bottom surfaces of the weld pool interface by Lamé curves, described in *2.2* and subsequently applied in *2.3* as an EHS, is shown in Fig. 3.

The steady-state temperature field provides information about the regions of the weld pool which solidify at last. Such regions are of main interest since the formation of hot cracking requires the presence of a liquid film between the grain boundaries. Thus, any geometrical characteristic of the weld pool interface can play a crucial role in the hot cracking formation.

A detailed analysis of the steady-state temperature field and the liquid-fraction shows how critical the bulge region can be. A longitudinal view of the weld pool geometry is shown in Fig. 2b. The solidification behavior of the liquid metal is studied in the cross-section S-S, see Fig. 2d. Three regions, highlighted by the points P_1, P_2, and P_3 show a delay in solidification. The delay in the middle of the cross-section is due to the bulge observed in the longitudinal section.

The presence of a liquid film between the grain boundaries leads to a decrease in the cracking resistivity in these regions. Thus, the bulge region can be identified as particularly susceptible to hot cracking, as it will be shown in the following subsections.

4.2. Influence of the bulge on the mechanical factor

The study of the influence of the bulge on the mechanical factor is based on the localized stress/strain across the grain boundary liquid film, which in turn causes the formation of cracks. In general, both localized stress and strain can be used to estimate the hot cracking susceptibility. Nevertheless, considering the high sheet thickness of the sample, the stress is used to evaluate the influence of the bulge on the hot cracking susceptibility in the presented model.

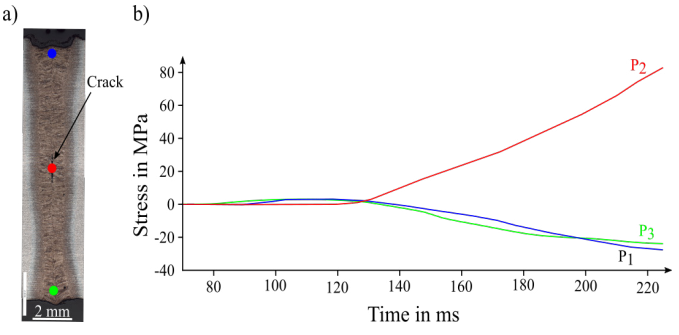

Fig. 4. a) An exemplary metallographic cross-section for 12 mm thick weld with a longitudinal crack and b) temporal distribution of the transversal horizontal stress at the locations P_1, P_2, and P_3 according to [21]

In *4.1* three regions are identified as critical since the melt solidifies there at last. Thus, the temporal transversal horizontal and vertical stress evolution during the cooling stage of the process in the three points P_1, P_2, and P_3 is studied. These points are marked on a metallographic cross-section with a longitudinal hot crack appearing in the bulge region, see Fig. 4a. The results of the temporal transversal horizontal stress evolution are presented in Fig. 4b. Note, that the stress-time curve at each of the three locations is highlighted by the same color as the corresponding point in Fig. 4a.

As can be seen from Fig. 4b the mechanical behavior at the locations P_1 and P_3 is almost identical. As the material starts solidifying a small increase of a tensile stress appears, which after a short period becomes compressive with a maximum value of approx. -30 MPa. In contrast to that, the transversal horizontal stress in the bulge region remains tensile during the solidification process. It shows a nearly linear increase of up to approx. 80 MPa at the corresponding Fe-S eutectic temperature of around 988 °C. Since the growth direction of the dendrites is opposite to the calculated transversal stresses, a rupture of the liquid film between the grain boundaries in the bulge region is very likely to occur.

4.3. Influence of the bulge on the metallurgical factor

The third dominant effect on hot cracking formation is the metallurgical factor. In general, the accumulation of sulfur ahead of the solid-liquid interface due to segregation and diffusion defines the local microstructure. In regions with locally increased sulfur content the hot cracking resistivity of the material decreases due to the extended solidification temperature range or with other words due to the extended dwell time of the liquid film between the grain boundaries.

In fact, two factors contribute to the local microstructure and material properties. The first factor is the concentration of impurities ahead of the solidification front and the second the direction of crystallization. Crystals converging to a small area contribute to the total local accumulation of sulfur, and thus further decrease the cracking resistivity.

The bulge on the weld pool interface influences both factors. It leads to more complex crystal geometries, irregular solidification rates and crystal cross-sectional profiles. Thus, the state of heterogeneity of the material can exceed the theoretical limit determined by the distribution factor and the initial concentration of the impurity. As an example, the case of sulfur with initial concentration C_0 and distribution factor 0.05 is considered. Assuming a constant solidification rate and cross-sectional profile the theoretical limit of the relative concentration is twenty times C_0. If the bulge effect on the solidification rate and the cross-sectional profile is included the limit can exceed this factor up to several times.

The impact of the bulge on the second factor is schematically explained in Fig. 5a and 5b. Based on the assumptions made in *2.6* the direction of crystallization coincides with the direction of the temperature gradient. Due to the bulge on the solid-liquid interface the crystals C_1, and C_3 (from above and below the bulge plane, respectively) will converge in the bulge plane. Thus, the accumulated sulfur ahead of the solid-liquid interface is pushed to the same area, leading to a further rise of the local sulfur concentration. This solidification behaviour is observed in the longitudinal section, see Fig. 5a, as well as in the cross-section, see Fig. 5b.

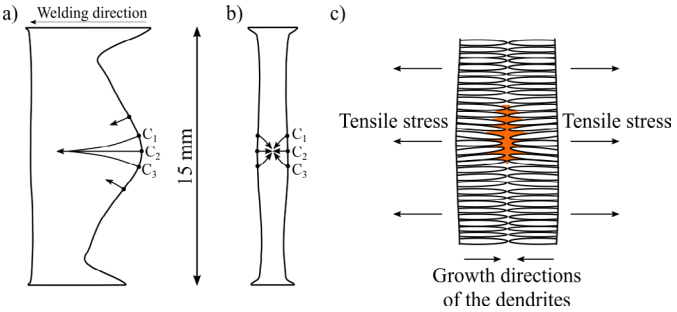

Fig. 5. Schematical projection of the crystal axis on a) the longitudinal section in the symmetry plane, b) the cross-section and c) increased hot cracking susceptibility due to the bulge effect according to [21]

The more sulfur accumulates the longer the dwell time of the liquid film between the grain boundaries will be. The extended dwell time increases the probability for the liquid film to be ruptured by the rising with time tensile stress in the bulge region, calculated in *4.2*, see Fig. 5c.

The bulge in the cross-section, see Fig. 5b, has an additional impact on the hot cracking formation. The larger distance between the seam flanks hinders the coalescence of the dendrite tips. The combination of this effect with the local tensile stress is a further indicator of increased hot cracking susceptibility in the bulge region, as shown schematically in Fig. 5c.

Considering all three effects of the bulge region on the local microstructure, its impact is identified to be critical for the cracking susceptibility of the material.

5. Conclusions

A coupled multiphysics, multiscale numerical framework is developed, comprising a series of subsequent analyses. The study examines the influences of the bulge on the three most dominant effects causing hot cracking, namely the thermal cycles, the mechanical loading, and the local microstructure.

The following conclusions are drawn from the obtained numerical and experimental results:

- Fluid flow effects lead to a bulge formation in the weld pool shape approximately in the middle of the plate.
- The bulge on the solid-liquid interface leads to a delay in the solidification behavior in the cracking region (steady-state solidification).
- The temperature loading due to the equivalent heat source results in maximum tensile stress around the melt in the bulge region. This can lead to a possible rupture of the liquid film between the grain boundaries.
- The solidification conditions become even more critical due to the accumulation of sulfur in the bulge region, caused by segregation, diffusion, and predominant crystals growth into the hot-cracking region.
- The bulge in the weld pool shape increases the hot cracking susceptibility by enhancing the three dominant effects.

Acknowledgements

Financial funding by the Deutsche Forschungsgemeinschaft (DFG, German Research Foundation) - project Nr. 411393804 (BA 5555/5-1) is gratefully acknowledged.

References

[1] J.F. Ready, D.F. Farson (Eds.). LIA Handbook of Laser Materials Processing. Laser Institute of America. Orlando; 2001.
[2] M. Bachmann, A. Gumenyuk, M. Rethmeier. Welding with high-power lasers: Trends and developments. Phys. Procedia 83; 2016. p. 15–25.
[3] X. Zhang, E. Ashida, S. Tarasawa, Y. Anma, M. Okada, S. Katayama, M. Mitzutani. Welding of thick stainless steel plates up to 50mm with high brightness lasers. J. Laser Appl. 23; 2011; 022002.
[4] A. Fritzsche, V. Avilov, A. Gumenyuk, K. Hilgenberg, M. Rethmeier, M. High power laser beam welding of thick-walled ferromagnetic steels with electromagnetic weld pool support. Physics Procedia; 2016; 83; p. 362–372.
[5] J. Schuster, S. Keitel, E. Schulze, H. Maly. Fachbeiträge-Entstehung erstarrungsbedingter Risse in Laserstrahlschweissverbindungen an unlegierten und niedriglegierten Baustahlen. Schweißen und Schneiden; 1999; 51; p. 252–257.
[6] J. Schuster. Heißrisse in Schweißverbindungen: Entstehung, Nachweis und Vermeidung. DVS-Verlag; 2004.
[7] M.O. Gebhardt, A. Gumenyuk, M. Rethmeier. Numerical analysis of hot cracking in laser hybrid welded tubes. Advances in Materials Science and Engineering; 2013; 520786.
[8] A. Artinov, N. Bakir, M. Bachmann, A. Gumenyuk M. Rethmeier. Weld pool shape observation in high power laser beam welding. Physics Procedia; 2018.
[9] M. Rappaz, J. Dantzig. Solidification, first, EFPL Press; 2009.
[10] J. Lippold. Welding Metallurgy and Weldability, first, John Wiley & Sons; 2014.
[11] G. Agarwal, A. Kumar, I.M. Richardson, M.J.M. Hermans. Evaluation of solidification cracking susceptibility during laser welding in advanced high strength automotive steels. Materials & Design; 2019; 183: 108104.
[12] J. Draxler, J. Edberg, J. Andersson, L.E. Lindgren. Modeling and simulation of weld solidification cracking part I. Welding in the World; 2019; 63(5); p. 1489–1502.
[13] S. Kou. Welding Metallurgy, second, John Wiley & Sons, Inc.; 2003.
[14] M.E. Glicksman. Principles of Solidification: An Introduction to Modern Casting and Crystal Growth Concepts. Springer New York; 2011.
[15] C. Cross. On the origin of weld solidification cracking. In Hot cracking phenomena in welds. Springer; 2005; p. 3–18.
[16] T. Shida, H. Okumura, Y. Kawada. Effects of welding parameters and prevention of defects in deep penetration electron beam welding of heavy section steel plates. Weld. World; 1979; 17; p. 196–207.
[17] S .Tsukamoto, H. Irie, M. Inagaki. Welding Defects and Molten Metal Behaviour in Electron Beam Welding. The fourth international Symposium of the Japan Welding Society; 1982; p. 115–120.
[18] S. Tsukamoto, H. Irie. Welding defects and molten metal behaviour in low speed electron beam welding. Welding in the World; 1985; 23; p. 130–140.
[19] S. Tsukamoto, H. Irie. Mechanism of locally delayed solidification in electron beam welding. Welding international; 1991; 5; p. 177–183.
[20] M.O. Gebhardt. Einfluss von Konstruktion und Schweißparametern auf die Erstarrungsrissentstehung beim Laser-MSG-Hybridschweißen dickwandiger Bauteile: experimentelle und numerische Analyse. Technische Universität Berlin; 2013.
[21] N. Bakir, A. Artinov, A. Gumenyuk, M. Bachmann, M. Rethmeier. Numerical simulation on the origin of solidification cracking in laser welded thick-walled structures. Metals; 2018; 8(6): 406.
[22] L.D. Barbetta. Solidification flaw and porosity formation in hybrid laser: GMA welding of thick API 5L X70 steel plates; 2014. (Master's thesis).
[23] L.D. Barbetta, W.L. Weingaertner, O. Seffer, R. Lahdo, S. Kaierle, S. Influence of molten pool geometry and process parameters on solidification cracsk formation in hybrid laser-GMA welding of thick 5L X70 steel plates; In ABCM International Congress of Manufacturing Engineering (COBEM), 8th Brazilian Congress of Manufacturing Engineering; Brazil; 2015.
[24] W.-I. Cho, S.-J. Na, C. Thomy, F. Vollertsen. Numerical simulation of molten pool dynamics in high power disk laser welding. Journal of Materials Processing Technology; 2012; 212; p. 262–275.
[25] M. Bachmann, V. Avilov, A. Gumenyuk, M. Rethmeier. Experimental and numerical investigation of an electromagnetic weld pool support system for high power laser beam welding of austenitic stainless steel. Journal of Materials Processing Technology; 2014; 214(3); p. 578–591.
[26] M. Bachmann, V. Avilov, A. Gumenyuk, M. Rethmeier. Experimental and numerical investigation of an electromagnetic weld pool control for laser beam welding. Physics Procedia; 2014; 56; p.515–524.
[27] M. Bachmann, R. Kunze, V. Avilov, M. Rethmeier. Finite element modeling of an alternating current electromagnetic weld pool support in full penetration laser beam welding of thick duplex stainless steel plates. Journal of Laser Applications; 2016; 28(2), p. 022404.
[28] F. Lu, X. Li, Z. Li, X. Tang, H. Cui. Formation and influence mechanism of keyhole-induced porosity in deep-penetration laser welding based on 3D transient modeling. International Journal of Heat and Mass Transfer; 2015; 90; p. 1143–1152.
[29] M. Sohail, S.-W. Han, S.-J. Na, A. Gumenyuk, M. Rethmeier. Numerical investigation of energy input characteristics for high-power fiber laser welding at different positions. International Journal of Advanced Manufacturing Technology; 2015; 80; p. 931–946.
[30] Z. Gao, P. Jiang, G. Mi, L. Cao, W. Liu. Investigation on the weld bead profile transformation with the keyhole and molten pool dynamic behavior simulation in high power laser welding. International Journal of Heat and Mass Transfer; 2018; 116; p. 1304–1313.
[31] A. Artinov, N. Bakir, M. Bachmann, A. Gumenyuk, M. Rethmeier. Weld pool shape observation in high power laser beam welding. Procedia CIRP; 2018; 74; p. 683–686.
[32] A. Artinov, N. Bakir, M. Bachmann, A. Gumenyuk, S.J. Na, M. Rethmeier. On the search for the origin of the bulge effect in high power laser beam welding. Journal of Laser Applications; 2019; 31(2); 022413.
[33] V. Pavelic. Experimental and computed temperature histories in gas tungsten arc welding of thin plates. Welding Journal Research Supplement; 1969; 48; p. 296–305.
[34] D. Radaj, H. Häuser, S. Braun. Numerische Simulation von Eigenspannungen und Verzug bei Schweißverbindungen aus AlMgSi-Legierungen. Konstruktion; 1998; 50(7-8); p. 31–37.
[35] M. Beck. Modellierung des Lasertiefschweißens. Teubner; 1996.
[36] R. Rai, S.M. Kelly, R.P. Martukanitz, T. DebRoy, T. A convective heat-transfer model for partial and full penetration keyhole mode laser welding of a structural steel. Metallurgical and Materials Transactions A; 2008; 39(1); p. 98–112.
[37] M. Bachmann, V. Avilov, A. Gumenyuk, M. Rethmeier. Numerical simulation of full-penetration laser beam welding of thick aluminium plates with inductive support. J. Phys. D Appl. Phys; 2011; 035201.
[38] A. Artinov, M. Bachmann, M. Rethmeier, Equivalent heat source approach in a 3D transient heat transfer simulation of full-penetration high power laser beam welding of thick metal plates, Int. J. Heat Mass Transf. 2018; 122; p. 1003–1013.
[39] A. Artinov, V. Karkhin, N. Bakir, X, Meng, M. Bachmann, A. Gumenyuk, M. Rethmeier. Lamé curves approximation for the assessment of the 3-D temperature distribution in keyhole mode welding processes. Journal of Laser Applications; 2020; 32; 022024.
[40] A. Artinov, V. Karkhin, P. Khomich, M. Bachmann, M. Rethmeier. Assessment of thermal cycles by combining thermo-fluid dynamics and heat conduction in keyhole mode welding processes. International Journal of Thermal Sciences; 2019; 145; 105981.
[41] K. Satoh, Y Ueda, H. Kiharak. Recent trend of researches on restraint stresses and strains for weld cracking.Trans. JWRI; 1972; 42; p. 53–68.
[42] V. A. Karkhin V. A. Thermal processes in welding. Springer; 2019.
[43] V.A. Karkhin, P.N. Khomich, P. Rayamaki. Analysis of chemical macroheterogeneity in the vicinity of the fusion boundary in fusion welding. Welding International; 2010; 24:2; p. 125–130.
[44] A. Artinov, V.A. Karkhin, M. Bachmann, M. Rethmeier. Mathematical modeling of the geometrical differences between the weld end crater and the steady-state weld pool. Journal of Laser Applications; 2020; 32; 022024.